

Gauge conditions for long-term numerical black hole evolutions without excision

Miguel Alcubierre^(1,2), Bernd Brügmann⁽¹⁾, Peter Diener⁽¹⁾, Michael Koppitz⁽¹⁾, Denis Pollney⁽¹⁾,
Edward Seidel^(1,3), and Ryoji Takahashi^(1,4)

⁽¹⁾ *Max-Planck-Institut für Gravitationsphysik, Albert-Einstein-Institut, Am Mühlenberg 1, 14476 Golm, Germany*

⁽²⁾ *Instituto de Ciencias Nucleares, Universidad Nacional Autónoma de México, A.P. 70-543, 04510 México, D. F., México.*

⁽³⁾ *National Center for Supercomputing Applications, Beckman Institute, 405 N. Mathews Ave., Urbana, IL 61801*

⁽⁴⁾ *Theoretical Astrophysics Center, Juliane Maries Vej 30, 2100 Copenhagen, Denmark*

(June 25, 2002; AEI-2002-037)

Numerical relativity has faced the problem that standard 3+1 simulations of black hole spacetimes without singularity excision and with singularity avoiding lapse and vanishing shift fail after an evolution time of around $30 - 40M$ due to the so-called slice stretching. We discuss lapse and shift conditions for the non-excision case that effectively cure slice stretching and allow run times of $1000M$ and more.

04.25.Dm, 04.30.Db, 95.30.Sf, 97.60.Lf

I. INTRODUCTION

A crucial role in numerical relativity simulations of two black holes (BH) is played by the choice of coordinates. This gauge choice involves both the choice of a lapse function and of a shift vector, which typically have to be determined dynamically during a numerical evolution. The first results for colliding BH's were obtained for head-on collisions using the ADM decomposition of the Einstein equations with the lapse determined by the maximal slicing condition and the shift vector set to zero [1–3]. Maximal slices are known to be singularity avoiding, that is, starting from BH initial data where the physical singularity is to the future of the initial hypersurface, the lapse approaches the Minkowski value of unity in the asymptotically flat regions, but approaches zero near the physical singularity. In this way one can in principle foliate a BH spacetime without singularities, but since time marches on in the far regions while being frozen in the interior, the slices become more and more distorted. Historically, this phenomenon has been called ‘grid stretching’ by the numerical relativity community, though we will refer to it as ‘slice stretching’ since it is a property of the slices themselves, quite independent of the existence of a numerical grid. Slice stretching introduces a difficult problem for numerical simulations since the metric develops large gradients that keep on growing until the numerical code can no longer handle them and fails. Advanced numerical methods can help in spherical symmetry, see, e.g., [4], but to date have not proved very successful in three-dimensional (3D) evolutions [5].

Nonetheless, such singularity avoiding slicings with vanishing shift have been quite successful, since they do allow a finite evolution time of roughly $t = 30 - 40M$ (with M the total ADM mass of the system) for fully 3D evolutions of BH's, as first demonstrated in 1995 for the case of a single Schwarzschild BH [6]. In [7] the first fully 3D simulation of the grazing collision of two nearby BH's was performed with singularity avoiding slicing and

vanishing shift, lasting for about $7M$. With improved techniques the grazing collision has recently been pushed to about $35M$, which for the first time allowed the extraction of gravitational waveforms from a 3D numerical merger [8]. And even though singularity avoiding slicings with vanishing shift have so far been limited to a finite time interval of only $30 - 40M$, this interval can be moved into the truly non-linear regime of a plunge starting from an approximate innermost stable circular orbit (ISCO) of two BH's, since the remainder of the merger and ring-down can be computed using the close limit approximation [9]. Following such an approach, the first waveforms for the plunge from an approximate ISCO have been obtained [10–12].

So far the most important strategy to avoid slice stretching has been black hole excision [13,14]. The idea is to use horizon penetrating coordinates (notice that maximal slicing *is* horizon penetrating unless one imposes the extra boundary condition of having a vanishing lapse at the horizon) and to excise the interior of the BH's from the numerical grid. A non-vanishing shift is essential to keep grid points from falling into the BH. This approach has seen many successful implementations for single black holes. First demonstrated in 3D in [6], with further development it has, in particular, allowed to move a black hole across the numerical grid [15]. If a stable numerical implementation can be found, this approach should make it possible to simulate many orbits of two well separated BH's. The key difference between BH excision and the use of singularity avoiding slicings with vanishing shift is that with excision single static BH's can be stably evolved for thousands of M ; see [15] for the case of evolutions using null coordinates (that do not directly generalize to binary BH systems), and recently $100,000M$ have been reached for a single BH with a 3+1 Cauchy code in octant symmetry [16]. Black hole excision holds a lot of promise, even if currently evolutions of only $9-15M$ have been achieved for binary BH's [17].

In this paper we demonstrate that the new lapse and

shift conditions introduced in [18] for the case of a single distorted BH with excision (using the excision techniques of [16]) can work well even *without excision*. This allows us to break through the barrier of about $35M$ for singularity avoiding slicings in 3+1 numerical relativity. Our gauge choice maintains singularity avoidance but cures the main problems associated with slice stretching, allowing us to reach $500M$ and more for the evolution of single or even distorted BH's. For BH's colliding head-on that merge early on during the evolution, i.e. which start out sufficiently close to each other, the final BH can again be evolved for hundreds or even thousands of M .

Moreover, these gauge conditions have two important effects: (a) they drive the system towards a static state, virtually, if not completely, eliminating the chronic growth in metric functions typical of slice stretching. Hence, in principle they should allow for indefinitely long evolutions (if no other instabilities develop; see below). (b) since unbounded growth in metric functions is halted, they allow *much more accurate* results to be obtained for extremely long times, and at lower resolution than before. Below we will show results obtained for colliding black holes that show only 10% error in the horizon mass after more than $5000M$ of evolution.

The evolutions in this paper are carried out using the puncture method for evolutions [7,6]. The starting point is initial data of the Brill-Lindquist topology in isotropic coordinates [19]. This ‘puncture’ data is defined on R^3 minus a point for each of the internal asymptotically flat ends of the BH's. If one treats the coordinate singularity at the punctures appropriately, the punctures do not evolve as long as the shift vanishes there. That is, the metric and the extrinsic curvature do not evolve at the punctures. It can also be checked that the maximal slicing equation produces a smooth numerical solution for the lapse at the punctures.

One basic observation for our choice of shift vector is that the ‘Gamma freezing’ shift introduced in [18] for our project in simple BH excision has the following property when the BH's are not excised but are represented as punctures: Initially the shift is zero, but as the slice stretching develops, the shift reacts by pulling out points from the inner asymptotically flat region near the punctures. The lapse and shift conditions taken together are then able to virtually stop the evolution of one or even two black holes, essentially mimicking the behavior of the lapse and shift known from stable evolutions of a BH in Kerr-Schild coordinates. This is a key result that will be detailed below.

The paper is organized as follows. First we introduce the evolution equations and the constraints in Section II. In Sec. III we discuss the gauge conditions. The puncture initial data and puncture evolutions are discussed in Sec. IV and Sec. V. In Sec. VI miscellaneous aspects of our numerical implementation are discussed. In Sec. VII we present numerical results for one and two BH's, and we conclude in Sec. VIII.

II. FORMULATION

The standard variables in the 3+1 formulation of ADM (Arnowitt-Deser-Misner, see [20]) are the 3-metric γ_{ij} and the extrinsic curvature K_{ij} . The gauge is determined by the lapse function α and the shift vector β^i . We will only consider the vacuum case. The evolution equations are

$$(\partial_t - \mathcal{L}_\beta) \gamma_{ij} = -2\alpha K_{ij}, \quad (1)$$

$$(\partial_t - \mathcal{L}_\beta) K_{ij} = -D_i D_j \alpha + \alpha(R_{ij} + K K_{ij} - 2K_{ik} K^k{}_j), \quad (2)$$

and the constraints are

$$\mathcal{H} \equiv R + K^2 - K_{ij} K^{ij} = 0, \quad (3)$$

$$\mathcal{D}^i \equiv D_j (K^{ij} - \gamma^{ij} K) = 0. \quad (4)$$

Here \mathcal{L}_β is the Lie derivative with respect to the shift vector β^i , D_i is the covariant derivative associated with the 3-metric γ_{ij} , R_{ij} is the three-dimensional Ricci tensor, R the Ricci scalar, and K is the trace of K_{ij} .

We will use the BSSN form of these equations (Baumgarte, Shapiro [21], and Shibata, Nakamura [22]). One introduces new variables based on a trace decomposition of the extrinsic curvature and a conformal rescaling of both the metric and the extrinsic curvature. The trace-free part A_{ij} of the extrinsic curvature is defined by

$$A_{ij} = K_{ij} - \frac{1}{3} \gamma_{ij} K. \quad (5)$$

Assuming that the metric γ_{ij} is obtained from a conformal metric $\tilde{\gamma}_{ij}$ by a conformal transformation,

$$\gamma_{ij} = \psi^4 \tilde{\gamma}_{ij}, \quad (6)$$

we can choose a conformal factor ψ such that the determinant of $\tilde{\gamma}_{ij}$ is 1:

$$\psi = \gamma^{1/12}, \quad (7)$$

$$\tilde{\gamma}_{ij} = \psi^{-4} \gamma_{ij} = \gamma^{-1/3} \gamma_{ij}, \quad (8)$$

$$\tilde{\gamma} = 1, \quad (9)$$

where γ is the determinant of γ_{ij} and $\tilde{\gamma}$ is the determinant of $\tilde{\gamma}_{ij}$. Instead of γ_{ij} and K_{ij} we can therefore use the variables

$$\phi = \ln \psi = \frac{1}{12} \ln \gamma, \quad (10)$$

$$K = \gamma_{ij} K^{ij}, \quad (11)$$

$$\tilde{\gamma}_{ij} = e^{-4\phi} \gamma_{ij}, \quad (12)$$

$$\tilde{A}_{ij} = e^{-4\phi} A_{ij}, \quad (13)$$

where $\tilde{\gamma}_{ij}$ has determinant 1 and \tilde{A}_{ij} has vanishing trace. Furthermore, we introduce the conformal connection functions

$$\tilde{\Gamma}^i = \tilde{\gamma}^{jk} \tilde{\Gamma}^i_{jk} = -\partial_j \tilde{\gamma}^{ij}, \quad (14)$$

where $\tilde{\Gamma}^i_{jk}$ is the Christoffel symbol of the conformal metric and where the second equality holds only if the determinant of the conformal 3-metric $\tilde{\gamma}$ is unity (which is true analytically but may not hold numerically). We call ϕ , K , $\tilde{\gamma}_{ij}$, \tilde{A}_{ij} , and $\tilde{\Gamma}^i$ the BSSN variables.

In terms of the BSSN variables the evolution equation (1) becomes

$$(\partial_t - \mathcal{L}_\beta) \tilde{\gamma}_{ij} = -2\alpha \tilde{A}_{ij}, \quad (15)$$

$$(\partial_t - \mathcal{L}_\beta) \phi = -\frac{1}{6}\alpha K, \quad (16)$$

while equation (2) leads to

$$(\partial_t - \mathcal{L}_\beta) \tilde{A}_{ij} = e^{-4\phi} [-D_i D_j \alpha + \alpha R_{ij}]^{TF} + \alpha (K \tilde{A}_{ij} - 2 \tilde{A}_{ik} \tilde{A}^k_j), \quad (17)$$

$$(\partial_t - \mathcal{L}_\beta) K = -D^i D_i \alpha + \alpha (\tilde{A}_{ij} \tilde{A}^{ij} + \frac{1}{3} K^2), \quad (18)$$

where TF denotes the trace-free part of the expression in brackets with respect to γ_{ij} . Note that the right-hand side of the evolution equation (17) for the trace-free variable \tilde{A}_{ij} is trace-free except for the term $\tilde{A}_{ik} \tilde{A}^k_j$. This is no contradiction since the condition that \tilde{A}_{ij} remains trace-free is $(\partial_t - \mathcal{L}_\beta) (\tilde{\gamma}^{ij} \tilde{A}_{ij}) = 0$ and not $\tilde{\gamma}^{ij} (\partial_t - \mathcal{L}_\beta) \tilde{A}_{ij} = 0$.

On the right-hand side of (18) we have used the Hamiltonian constraint (3) to eliminate the Ricci scalar,

$$R = K_{ij} K^{ij} - K^2 = \tilde{A}_{ij} \tilde{A}^{ij} - \frac{2}{3} K^2. \quad (19)$$

The momentum constraint (4) becomes

$$\partial_j \tilde{A}^{ij} = -\tilde{\Gamma}^i_{jk} \tilde{A}^{jk} - 6 \tilde{A}^{ij} \partial_j \phi + \frac{2}{3} \tilde{\gamma}^{ij} \partial_j K. \quad (20)$$

An evolution equation for $\tilde{\Gamma}^i$ can be obtained from (14) and (15),

$$\partial_t \tilde{\Gamma}^i = -2 \left(\alpha \partial_j \tilde{A}^{ij} + \tilde{A}^{ij} \partial_j \alpha \right) - \partial_j (\mathcal{L}_\beta \tilde{\gamma}^{ij}), \quad (21)$$

where we will use the momentum constraint above to substitute for the divergence of \tilde{A}^{ij} . One subtlety in obtaining numerically stable evolutions with the BSSN variables is precisely the question of how the constraints are used in the evolution equations. Several choices are possible and have been studied, see e.g. [23].

Note that in the preceding equations we are computing Lie derivatives of tensor densities. If the weight of a tensor density T is w , i.e. if T is a tensor times $\gamma^{w/2}$, then

$$\mathcal{L}_\beta T = [\mathcal{L}_\beta T]_{\partial}^{w=0} + w T \partial_k \beta^k, \quad (22)$$

where the first term denotes the tensor formula for Lie derivatives with the derivative operator ∂ and the second is the additional contribution due to the density factor. The density weight of $\psi = e^\phi$ is $\frac{1}{6}$, so the weight of $\tilde{\gamma}_{ij}$ and \tilde{A}_{ij} is $-\frac{2}{3}$ and the weight of $\tilde{\gamma}^{ij}$ is $\frac{2}{3}$. To be explicit,

$$\mathcal{L}_\beta \phi = \beta^k \partial_k \phi + \frac{1}{6} \partial_k \beta^k, \quad (23)$$

$$\mathcal{L}_\beta \tilde{\gamma}_{ij} = \beta^k \partial_k \tilde{\gamma}_{ij} + \tilde{\gamma}_{ik} \partial_j \beta^k + \tilde{\gamma}_{jk} \partial_i \beta^k - \frac{2}{3} \tilde{\gamma}_{ij} \partial_k \beta^k, \quad (24)$$

$$\mathcal{L}_\beta \tilde{\gamma}^{ij} = \beta^k \partial_k \tilde{\gamma}^{ij} - \tilde{\gamma}^{ik} \partial_k \beta^j - \tilde{\gamma}^{jk} \partial_k \beta^i + \frac{2}{3} \tilde{\gamma}^{ij} \partial_k \beta^k. \quad (25)$$

The evolution equation (21) for $\tilde{\Gamma}^i$ therefore becomes

$$\begin{aligned} \partial_t \tilde{\Gamma}^i &= \tilde{\gamma}^{jk} \partial_j \partial_k \beta^i + \frac{1}{3} \tilde{\gamma}^{ij} \partial_j \partial_k \beta^k \\ &+ \beta^j \partial_j \tilde{\Gamma}^i - \tilde{\Gamma}^j \partial_j \beta^i + \frac{2}{3} \tilde{\Gamma}^i \partial_j \beta^j \\ &- 2 \tilde{A}^{ij} \partial_j \alpha + 2\alpha (\tilde{\Gamma}^i_{jk} \tilde{A}^{jk} + 6 \tilde{A}^{ij} \partial_j \phi - \frac{2}{3} \tilde{\gamma}^{ij} \partial_j K). \end{aligned} \quad (26)$$

In the second line we see the formula for a vector density of weight $\frac{2}{3}$, but since $\tilde{\Gamma}^i$ is not really a tensor density but is derived from Christoffel symbols we obtain extra terms involving second derivatives of the shift (the first line in the equation above).

On the right-hand sides of the evolution equations for \tilde{A}_{ij} and K , (17) and (18), there occur covariant derivatives of the lapse function, and the Ricci tensor of the non-conformal metric. Since

$$\Gamma^k_{ij} = \tilde{\Gamma}^k_{ij} + 2(\delta^k_i \partial_j \phi + \delta^k_j \partial_i \phi - \tilde{\gamma}_{ij} \tilde{\gamma}^{kl} \partial_l \phi), \quad (27)$$

where $\tilde{\Gamma}^k_{ij}$ is the Christoffel symbol of the conformal metric, we have for example

$$D^i D_i \alpha = e^{-4\phi} (\tilde{\gamma}^{ij} \partial_i \partial_j \alpha - \tilde{\Gamma}^k \partial_k \alpha + 2 \tilde{\gamma}^{ij} \partial_i \phi \partial_j \alpha). \quad (28)$$

The Ricci tensor can be separated in two parts,

$$R_{ij} = \tilde{R}_{ij} + R_{ij}^\phi, \quad (29)$$

where \tilde{R}_{ij} is the Ricci tensor of the conformal metric and R_{ij}^ϕ denotes additional terms depending on ϕ :

$$\begin{aligned} R_{ij}^\phi &= -2 \tilde{D}_i \tilde{D}_j \phi - 2 \tilde{\gamma}_{ij} \tilde{D}^k \tilde{D}_k \phi \\ &+ 4 \tilde{D}_i \phi \tilde{D}_j \phi - 4 \tilde{\gamma}_{ij} \tilde{D}^k \phi \tilde{D}_k \phi, \end{aligned} \quad (30)$$

with \tilde{D}_i the covariant derivative associated with the conformal metric. The conformal Ricci tensor can be written in terms of the conformal connection functions as

$$\begin{aligned} \tilde{R}_{ij} &= -\frac{1}{2} \tilde{\gamma}^{lm} \partial_l \partial_m \tilde{\gamma}_{ij} + \tilde{\gamma}_{k(i} \partial_{j)} \tilde{\Gamma}^k + \tilde{\Gamma}^k \tilde{\Gamma}_{(ij)k} \\ &+ \tilde{\gamma}^{lm} \left(2 \tilde{\Gamma}^k_{l(i} \tilde{\Gamma}_{j)km} + \tilde{\Gamma}^k_{im} \tilde{\Gamma}_{klj} \right). \end{aligned} \quad (31)$$

A key observation here is that if one introduces the $\tilde{\Gamma}^i$ as independent variables, then the principal part of the right-hand side of equation (17) contains the wave operator $\tilde{\gamma}^{lm}\partial_l\partial_m\tilde{\gamma}_{ij}$ but no other second derivatives of the conformal metric. This brings the evolution system one step closer to being hyperbolic.

One of the reasons why we have written out the BSSN system in such detail is to point out a subtlety that arises in the actual implementation if one wants to achieve numerical stability. In the computer code we do not use the numerically evolved $\tilde{\Gamma}^i$ in all places, but follow this rule:

- Partial derivatives $\partial_j\tilde{\Gamma}^i$ are computed as finite differences of the independent variables $\tilde{\Gamma}^i$ that are evolved using (26).
- In all expressions that just require $\tilde{\Gamma}^i$ and not its derivative we substitute $\tilde{\gamma}^{jk}\tilde{\Gamma}^i_{,jk}(\tilde{\gamma})$, that is we do not use the independently evolved variable $\tilde{\Gamma}^i$ but recompute $\tilde{\Gamma}^i$ according to its definition (14) from the current values of $\tilde{\gamma}_{ij}$.

In practice we have found that the evolutions are far less stable if either $\tilde{\Gamma}^i$ is treated as an independent variable everywhere, or if $\tilde{\Gamma}^i$ is recomputed from $\tilde{\gamma}_{ij}$ before each time step. The rule just stated helps to maintain the constraint $\tilde{\Gamma}^i = -\partial_j\tilde{\gamma}^{ij}$ well behaved without removing the advantage of reformulating the principal part of the Ricci tensor.

In summary, we evolve the BSSN variables $\tilde{\gamma}_{ij}$, ϕ , \tilde{A}_{ij} , K , and $\tilde{\Gamma}^i$ according to (15), (16), (17), (18), and (26), respectively. The Ricci tensor is separated as shown in (29) with each part computed according to (30) and (31) respectively. The Hamiltonian and momentum constraints have been used to write the equations in a particular way. The evolved variables $\tilde{\Gamma}^i$ are only used when their partial derivatives are needed (the one term in the conformal Ricci tensor (31) and the advection term $\beta^k\partial_k\tilde{\Gamma}^i$ in the evolution equation for the $\tilde{\Gamma}^i$ themselves, Eq. (26)).

III. THE GAUGE CONDITIONS

We will consider families of gauge conditions that are not restricted to puncture data and that can be used in principle with any 3+1 form of the Einstein's equations that allows a general gauge. However, the specific family we test in this paper is best motivated by considering the BSSN system introduced above. For the present purposes, of special importance are the following two properties of this formulation:

- The trace of the extrinsic curvature K is treated as an independent variable. For a long time it has been known that the evolution of K is directly related to the choice of a lapse function α . Thus, having K as an independent field allows one to impose slicing conditions in a much cleaner way.

- The appearance of the “conformal connection functions” $\tilde{\Gamma}^i$ as independent quantities. As already noted by Baumgarte and Shapiro [21] (see also [24,25]), the evolution equation for these quantities can be turned into an elliptic condition on the shift which is related to the minimal distortion condition. More generally, one can relate the shift choice to the evolution of these quantities, again allowing for a clean treatment of the shift condition.

Our aim is to look for gauge conditions that at late times, once the physical system under consideration has settled to a final stationary state, will be able to drive the coordinate system to a frame where this stationarity is evident. In effect, we are looking for “symmetry seeking” coordinates of the type discussed by Gundlach and Garfinkle and also by Brady, Creighton, and Thorne [26,27] that will be able to find the approximate Killing field that the system has at late times. In order to achieve this we believe that the natural approach is to relate the gauge choice to the evolution of certain combinations of dynamic quantities in such a way that the gauge will either freeze completely the evolution of those quantities (typically by solving some elliptic equations), or will attempt to do so with some time delay (by solving instead parabolic or hyperbolic equations).

We will consider the lapse and shift conditions in turn. Special cases of the gauge conditions that we will introduce here were recently used together with BH excision with remarkable results in [16], but as we will show below, the conditions are so powerful that in the cases tested, they work *even without excision*.

A. Slicing conditions

The starting point for our slicing conditions is the “ K -freezing” condition $\partial_t K=0$, which in the particular case when $K=0$ reduces to the well known “maximal slicing” condition. The K -freezing condition leads to the following elliptic equation for the lapse:

$$\Delta\alpha = \beta^i\partial_i K + \alpha K_{ij}K^{ij}, \quad (32)$$

with Δ the Laplacian operator for the spatial metric γ_{ij} . In the BSSN formulation, once we have solved the elliptic equation for the lapse, the K -freezing condition can be imposed at the analytic level by simply not evolving K .

One can construct parabolic or hyperbolic slicing conditions by making either $\partial_t\alpha$ or $\partial_t^2\alpha$ proportional to $\partial_t K$. We call such conditions “ K -driver” conditions (see [28]). The hyperbolic K -driver condition has the form [4,18]

$$\partial_t\alpha = -\alpha^2 f(\alpha)(K - K_0), \quad (33)$$

where $f(\alpha)$ is an arbitrary positive function of α and $K_0 = K(t=0)$. In our evolutions, we normally take

$$f(\alpha) = \frac{2}{\alpha}, \quad (34)$$

which is referred to as 1+log slicing, since empirically we have found that such a choice has excellent singularity avoiding properties. In Sec. IV B we introduce a modification of $f(\alpha)$ for puncture evolutions. The hyperbolic K-driver condition is in fact only a slight generalization of the Bona-Masso family of slicing conditions [4]: $\partial_t \alpha = -\alpha^2 f(\alpha) K$.

By taking an extra time derivative of the slicing condition above, and using the evolution equation for K , one can see that the lapse obeys a generalized wave equation,

$$\begin{aligned} \partial_t^2 \alpha &= -\partial_t(\alpha^2 f)(K - K_0) - \alpha^2 f \partial_t K \\ &= \alpha^2 f(\Delta \alpha - \alpha K_{ij} K^{ij} - \beta^i D_i K + 2\alpha f + \alpha^2 f'). \end{aligned} \quad (35)$$

Previously we have also experimented with a somewhat different form of hyperbolic K-driver condition

$$\partial_t^2 \alpha = -\alpha^2 f \partial_t K, \quad (36)$$

where the right hand side vanishes in the case that K freezing is achieved. However, one may anticipate the problem that even in the case when $\partial_t K = 0$ we only obtain $\partial_t \alpha = \text{const}$, while for (33) we see that $K = \dot{K}_0$ implies that $\partial_t \alpha = 0$. Moreover, in black hole evolutions where the lapse collapses to zero, condition (33) guarantees that the lapse will stop evolving, while condition (36) only implies that $\partial_t \alpha$ will stop evolving so the lapse can easily “collapse” beyond zero and become negative. For these reasons, in practice the condition Eq. (33) leads to more stable black hole evolutions, and this is the slicing condition that we consider in this paper.

The wave speed in both cases is $v_\alpha = \alpha \sqrt{f(\alpha)}$, which explains the need for $f(\alpha)$ to be positive. Notice that, depending on the value of $f(\alpha)$, this wave speed can be larger or smaller than the physical speed of light. This represents no problem, as it only indicates the speed of propagation of the coordinate system, i.e. it is only a “gauge speed”. In particular, for the 1+log slicing introduced above with $f = 2/\alpha$, the gauge speed in the asymptotic regions (where $\alpha \simeq 1$) becomes $v_\alpha = \sqrt{2} > 1$. One could then argue that choosing $f = 1/\alpha$ should be a better alternative, as the asymptotic gauge speed would then be equal to the physical speed of light. However, experience has shown that such a choice is not nearly as robust and seems to lead easily to gauge pathologies as those studied in [29,30].

B. Shift conditions

In the BSSN formulation, an elliptic shift condition is easily obtained by imposing the “Gamma-freezing” condition $\partial_t \tilde{\Gamma}^k = 0$, or using (26),

$$\begin{aligned} &\tilde{\gamma}^{jk} \partial_j \partial_k \beta^i + \frac{1}{3} \tilde{\gamma}^{ij} \partial_j \partial_k \beta^k - \tilde{\Gamma}^j \partial_j \beta^i + \frac{2}{3} \tilde{\Gamma}^i \partial_j \beta^j + \beta^j \partial_j \tilde{\Gamma}^i \\ &- 2\tilde{A}^{ij} \partial_j \alpha - 2\alpha \left(\frac{2}{3} \tilde{\gamma}^{ij} \partial_j K - 6\tilde{A}^{ij} \partial_j \phi - \tilde{\Gamma}_{jk}^i \tilde{A}^{jk} \right) = 0. \end{aligned} \quad (37)$$

Notice that, just as it happened with the K -freezing condition for the lapse, once we have solved the previous elliptic equations for the shift, the Gamma-freezing condition can be enforced at an analytic level by simply not evolving the $\tilde{\Gamma}^k$.

The Gamma-freezing condition is closely related to the well known minimal distortion shift condition [31]. In order to see exactly how these two shift conditions are related, we write here the minimal distortion condition

$$\nabla_j \Sigma^{ij} = 0, \quad (38)$$

where Σ_{ij} is the so-called “distortion tensor” defined as

$$\Sigma_{ij} := \frac{1}{2} \gamma^{1/3} \partial_t \tilde{\gamma}_{ij}, \quad (39)$$

with $\tilde{\gamma}_{ij}$ the same as before. A little algebra shows that the evolution equation for the conformal connection functions (26) can be written in terms of Σ_{ij} as

$$\partial_t \tilde{\Gamma}^i = 2\partial_j \left(\gamma^{1/3} \Sigma^{ij} \right). \quad (40)$$

More explicitly, we have

$$\partial_t \tilde{\Gamma}^i = 2e^{4\phi} \left[\nabla_j \Sigma^{ij} - \tilde{\Gamma}_{jk}^i \Sigma^{jk} - 6\Sigma^{ij} \partial_j \phi \right]. \quad (41)$$

We then see that the minimal distortion condition $\nabla^j \Sigma_{ij} = 0$, and the Gamma-freezing condition $\partial_t \tilde{\Gamma}^i = 0$ are equivalent up to terms involving first spatial derivatives of the spatial metric multiplied with the distortion tensor itself. In particular, all terms involving second derivatives of the shift are identical in both cases (but not so terms with first derivatives of the shift which appear in the distortion tensor Σ_{ij}). That the difference between both conditions involves Christoffel symbols should not be surprising since the minimal distortion condition is covariant while the Gamma-freezing condition is not.

Just as it is the case with the lapse, we obtain parabolic and hyperbolic shift prescriptions by making either $\partial_t \beta^i$ or $\partial_t^2 \beta^i$ proportional to $\partial_t \tilde{\Gamma}^i$. We call such conditions “Gamma-driver” conditions. The parabolic Gamma driver condition has the form

$$\partial_t \beta^i = F_p \partial_t \tilde{\Gamma}^i, \quad (42)$$

where F_p is a positive function of space and time. In analogy to the discussion of the hyperbolic K-driver condition there are two types of hyperbolic Gamma-driver conditions that we have considered,

$$\partial_t^2 \beta^i = F \partial_t \tilde{\Gamma}^i - \eta \partial_t \beta^i, \quad (43)$$

or alternatively,

$$\partial_t^2 \beta^i = F \partial_t \tilde{\Gamma}^i - \left(\eta - \frac{\partial_t F}{F} \right) \partial_t \beta^i, \quad (44)$$

where F and η are positive functions of space and time. For the hyperbolic Gamma-driver conditions we have

found it crucial to add a dissipation term with coefficient η to avoid strong oscillations in the shift. Experience has shown that by tuning the value of this dissipation coefficient we can manage to almost freeze the evolution of the system at late times.

The rationale behind the two almost identical choices of Gamma-driver is the following. First note that if F is independent of time, the two choices are identical. However, we typically choose F to be proportional to α^p , with p some positive power (usually $p = 1$). Anticipating a collapsing lapse near the black hole this implies that the term $F\partial_t\tilde{\Gamma}^i$ approaches zero and the evolution of the shift tends to freeze independent of the behaviour and numerical errors of $\partial_t\tilde{\Gamma}^i$. We implement the first choice of the Gamma-driver, (43), as

$$\partial_t\beta^i = B^i, \quad \partial_t B^i = F\partial_t\tilde{\Gamma}^i - \eta B^i, \quad (45)$$

and the second choice, (44), as

$$\partial_t\beta^i = FB^i, \quad \partial_t B^i = \partial_t\tilde{\Gamma}^i - \eta B^i. \quad (46)$$

The second variant has the advantage that if F approaches zero due to the collapse of the lapse near a black hole, then $\partial_t\beta^i$ also approaches zero and the shift freezes. With the first variant, on the other hand, it is only $\partial_t B^i = \partial_t^2\beta^i$ the one that approaches zero, which means the shift can still evolve. Both Gamma-drivers can give stable black hole evolutions, although the second one leads to less evolution near the black holes.

An important point that needs to be considered when using the hyperbolic Gamma-driver condition is that of the gauge speeds. Just as it happened with the lapse, the use of a hyperbolic equation for the shift introduces new ‘‘gauge speeds’’ associated with the propagation of the shift. In order to get an idea of how these gauge speeds behave, we will consider for a moment the shift condition (43) for small perturbations of flat space (and taking $\eta=0$). From the form of $\partial_t\tilde{\Gamma}^i$ given by equation (26) we see that in such a limit the principal part of the evolution equation for the shift reduces to

$$\partial_t^2\beta^i = F \left(\delta^{jk}\partial_j\partial_k\beta^i + \frac{1}{3}\delta^{ij}\partial_j\partial_k\beta^k \right). \quad (47)$$

Consider now only derivatives in a given direction, say x . We find

$$\partial_t^2\beta^i = F \left(\partial_x^2\beta^i + \frac{1}{3}\delta^{ix}\partial_x\partial_x\beta^x \right), \quad (48)$$

which implies

$$\partial_t^2\beta^x = \frac{4}{3}F\partial_x^2\beta^x, \quad (49)$$

$$\partial_t^2\beta^q = F\partial_x^2\beta^q \quad q \neq x. \quad (50)$$

We can then see that in regions where the spacetime is almost flat, the longitudinal part of the shift propagates with speed $v_{\text{long}} = 2\sqrt{F/3}$ while the transverse

part propagates with speed $v_{\text{trans}} = \sqrt{F}$. We therefore choose

$$F(\alpha) = \frac{3}{4}\alpha, \quad (51)$$

in order to have the longitudinal part of the shift propagate with the speed of light. The transverse part will propagate at a different speed, but its contribution far away is typically very small.

In the next section we will turn to puncture evolutions. Both $f(\alpha)$ and $F(\alpha)$ will be further adjusted for the presence of punctures.

IV. PUNCTURES

So far our discussion of the BSSN formulation and the proposed gauge conditions was quite independent of any particular choice of initial data, except that our gauge conditions are tailored for the late time stationarity of binary black hole mergers even though they are also applicable in more general situations. In this Section we introduce puncture initial data for black holes and the method of puncture evolutions.

A. Puncture initial data

Consider the three-manifold R^3 with one or more points (x_A, y_A, z_A) removed. These points we call punctures. The punctured R^3 arises naturally in solutions to the constraints in the Lichnerowicz-York conformal method [32,20] for the construction of black hole initial data. In the conformal method, we introduce on the initial hypersurface at $t = 0$ the conformal variables $\tilde{\gamma}_{ij}$ and \tilde{A}_{ij} by

$$\gamma_{ij} = \psi_0^4 \tilde{\gamma}_{ij}, \quad (52)$$

$$A_{ij} = \psi_0^{-2} \tilde{A}_{ij}, \quad (53)$$

where ψ_0 is the conformal factor, and leave K untransformed. Note that $\tilde{A}_{ij} = \psi_0^{-6} \tilde{A}_{ij}$ at $t = 0$.

Consider initial data with the conformally flat metric

$$\gamma_{ij} = \psi_0^4 \delta_{ij}. \quad (54)$$

Assuming that the extrinsic curvature K_{ij} vanishes, the momentum constraints (4) are trivially satisfied and the Hamiltonian constraint (3) reduces to

$$\Delta^\delta \psi_0 = 0, \quad (55)$$

where Δ^δ is the flat space Laplacian. A particular solution to this equation is

$$\psi_0 = 1 + \frac{m}{2r}, \quad (56)$$

where $r^2 = x^2 + y^2 + z^2$ and we assume $r \neq 0$. This way we have obtained initial data representing a slice of a

Schwarzschild black hole of mass m in spatially isotropic coordinates on a punctured R^3 . The horizon is located at $r = m/2$. There are two asymptotically flat regions, one for $r \rightarrow \infty$ and a second one at $r \rightarrow 0$. In fact, the metric is isometric under $r' = m^2/(4r)$. Since (55) is linear in ψ_0 one immediately obtains solutions for multiple black holes, for example

$$\psi_{BL} = 1 + \frac{m_1}{2r_1} + \frac{m_2}{2r_2}, \quad (57)$$

where $r_A^2 = (x - x_A)^2 + (y - y_A)^2 + (z - z_A)^2$ on an R^3 with two punctures at (x_A, y_A, z_A) , $A = 1, 2$. These solutions were first mentioned in [33] and studied in detail by Brill and Lindquist in [19]. While no longer isometric, this initial data contains one or two black holes depending on the separation of the punctures, but in any case with two separate inner asymptotic regions at the punctures. In particular, there is no physical singularity at the punctures, but there is a coordinate singularity at each puncture if one considers the unpunctured R^3 .

Brill-Lindquist data can be generalized to longitudinal, non-vanishing extrinsic curvature K_{ij} for multiple black holes with linear momentum and spin [34,35]. Here one uses the Bowen-York extrinsic curvature,

$$\begin{aligned} \bar{A}^{ij} &= \frac{3}{2r^2} (n^i P^j + n^j P^i - (\delta^{ij} - n^i n^j)) \delta_{kl} n^k P^l \\ &+ \frac{3}{r^3} (n^i \epsilon^{jkl} S_k n_l + n^j \epsilon^{ikl} S_k n_l), \end{aligned} \quad (58)$$

and $K = 0$. The parameters P^i and S^i are the linear and angular ADM momentum, and $n^i = x^i/r$ is the coordinate normal vector. The sum of two Bowen-York terms centered at two punctures is an explicit solution to the conformal momentum constraint with $K = 0$.

The key observation for puncture initial data is that, even though there is a coordinate singularity at each puncture, both in the conformal factor and in the Bowen-York extrinsic curvature, we can rewrite the Hamiltonian constraint as a regular equation on R^3 without any puncture points removed. This equation possesses a unique solution u that is C^2 at the punctures and C^∞ elsewhere, and the original Hamiltonian constraint is solved by

$$\psi_0 = u + \psi_{BL}. \quad (59)$$

Working on R^3 simplifies the numerical solution of the constraints over methods that for example use an isometry condition at the throat of a black hole.

Note that the puncture method for initial data can be applied using a conformally flat metric and the Kerr extrinsic curvature [36], and also to non-conformally flat initial data for multiple Kerr black holes [37–39]. In this paper we restrict ourselves to the conformally flat puncture data with Bowen-York extrinsic curvature.

B. Puncture evolutions in the ADM system

In this section we want to argue that one can obtain regular evolutions of puncture initial data without removing a region containing the puncture coordinate singularity from the grid by, say, an isometry condition at the throat of the black holes as in [3], or through black hole excision [13,14]. Evolving on R^3 instead of on R^3 with a sphere removed and an additional boundary condition imposed results in a significant technical simplification.

That this is possible was first noticed experimentally for a single Schwarzschild puncture in [6] for ADM evolutions with singularity avoiding slicing and vanishing shift. By turning off the isometry condition at the throat and computing everywhere including next to the puncture, the lapse equation can still be solved for a numerically smooth lapse with vanishing first derivative at the puncture that collapses to zero at and around the puncture during the evolution. The numerical grid in these simulations is staggered around the puncture points.

In [7], puncture evolutions are proposed as a general method for the evolution of the conformally flat, longitudinal extrinsic curvature data of orbiting and spinning black holes discussed in Sec. IV A. In particular, an argument is given that *the punctures do not evolve by construction*. This is not a theorem about the regularity of the solutions, as is available for puncture initial data [34,35], but it is consistent with the numerical results.

The basic idea is to examine the evolution equations and the gauge conditions at $t = 0$ in the limit of small distance to one of the punctures. For simplicity we move one of the punctures onto the origin and consider the limit $r \rightarrow 0$.

In this Section we will give a detailed version of the argument of [7] for the ADM equations with maximal slicing and vanishing shift, and then discuss the BSSN equations in Sec. IV C. First note that for the puncture initial data based on (58) and (59) we have $\psi_{BL} = O(1/r)$ and $u = O(1)$, and therefore at $t = 0$,

$$\psi_0 = O(1/r), \quad (60)$$

$$\psi_0^{-1} = O(r), \quad (61)$$

$$\gamma_{ij} = \psi_0^4 \delta_{ij} = O(1/r^4), \quad (62)$$

$$K_{ij} = \psi_0^{-2} \bar{A}_{ij} = O(1/r). \quad (63)$$

We therefore observe that the ADM equations (1) and (2) for the evolution of the metric and the extrinsic curvature are singular at the punctures.

The basic construction in puncture evolutions is to factor out the *time-independent* conformal factor ψ_{BL} (and not ψ_0) given by the initial data,

$$\gamma_{ij} = \psi_{BL}^4 \tilde{\gamma}_{ij}, \quad (64)$$

$$K_{ij} = \psi_{BL}^4 \tilde{K}_{ij}. \quad (65)$$

The key difference to the BSSN rescaling is that puncture evolutions involve a special rescaling that is independent of time.

Eq. (64) gives rise to a method for accurate finite differencing of the metric. For example, for the first partial derivative we have

$$\partial_k \gamma_{ij} = \psi_{BL}^4 \partial_k \tilde{\gamma}_{ij} + \tilde{\gamma}_{ij} \partial_k \psi_{BL}^4, \quad (66)$$

where ψ_{BL}^4 and $\partial_k \psi_{BL}^4$ are given analytically, and $\tilde{\gamma}_{ij}$ and $\partial_k \tilde{\gamma}_{ij}$ are assumed to remain regular during the evolution. By staggering the puncture between grid points one can therefore still obtain accurate derivatives of γ_{ij} near the puncture, and this applies to all quantities derived from the metric and its derivatives like the Christoffels and the Ricci tensor. In particular, there is no finite differencing across the singularity of $1/r$ terms.

In general, we have $\psi_0 = u + \psi_{BL}$ and the analytic derivatives of ψ_0 are not known, but we can still factor out ψ_{BL} as in (64) and (65) and obtain regular initial data,

$$\tilde{\gamma}_{ij} = \psi_{BL}^{-4} \psi_0^4 \delta_{ij} = O(1), \quad (67)$$

$$\tilde{K}_{ij} = \psi_{BL}^{-4} \psi_0^{-2} \tilde{A}_{ij} = O(r^3). \quad (68)$$

The question is whether $\tilde{\gamma}_{ij}$ and \tilde{K}_{ij} develop a singularity during the course of the evolution.

The ADM equations for $\tilde{\gamma}_{ij}$ and \tilde{K}_{ij} in the case of vanishing shift are

$$\partial_t \tilde{\gamma}_{ij} = -2\alpha \tilde{K}_{ij}, \quad (69)$$

$$\begin{aligned} \partial_t \tilde{K}_{ij} = & \psi_{BL}^{-4} (-D_i D_j \alpha + \alpha R_{ij}) \\ & + \tilde{\gamma}^{kl} (\tilde{K}_{ij} \tilde{K}_{kl} - 2\tilde{K}_{ik} \tilde{K}_{jl}). \end{aligned} \quad (70)$$

Let us examine the terms on the right hand side of the $\partial_t \tilde{K}_{ij}$ equation. For $\tilde{\gamma}_{ij} = O(1)$ and $\tilde{K}_{ij} = O(r^n)$, the terms involving \tilde{K}_{ij} are of order $O(r^{2n})$. According to (27), $\Gamma_{ij}^k = \tilde{\Gamma}_{ij}^k + (\Gamma_{\psi_{BL}}^k)_{ij}$. Assuming that $\tilde{\gamma}_{ij}$ and its derivatives are $O(1)$, we have $\tilde{\Gamma}_{ij}^k = O(1)$, but $(\Gamma_{\psi_{BL}}^k)_{ij} = O(1/r)$. Hence $\Gamma_{ij}^k = O(1/r)$, and similarly $R_{ij} = O(1/r^2)$. Finally, let us also assume that the lapse and its derivatives are of order $O(1)$. Then $\psi_{BL}^{-4} D_i D_j \alpha = O(r^3)$.

With these assumptions we obtain for $t = 0$ that

$$\partial_t \tilde{\gamma}_{ij}(0) = O(r^3), \quad (71)$$

$$\partial_t \tilde{K}_{ij}(0) = O(r^2), \quad (72)$$

where the $O(r^2)$ in the last equation is contributed by the term involving the Ricci tensor, the lapse terms are $O(r^3)$, and the extrinsic curvature terms are $O(r^6)$. In order to study the time evolution, we can perform one finite differencing step in time from $t = 0$ to $t = \Delta t$, for example,

$$\tilde{\gamma}_{ij}(\Delta t) = \tilde{\gamma}_{ij}(0) + \Delta t \partial_t \tilde{\gamma}_{ij}(0) = O(1), \quad (73)$$

$$\tilde{K}_{ij}(\Delta t) = \tilde{K}_{ij}(0) + \Delta t \partial_t \tilde{K}_{ij}(0) = O(r^2). \quad (74)$$

Note that \tilde{K}_{ij} has dropped from $O(r^3)$ to $O(r^2)$. However, it is readily checked that a second finite time step does not further lower the order of any variable since the order of the right hand side in the evolution equation of \tilde{K}_{ij} is dominated by $\psi_{BL}^{-4} R_{ij}$. We therefore find that

$$\tilde{\gamma}_{ij}(t) = O(1), \quad \partial_t \tilde{\gamma}_{ij}(t) = O(r^2), \quad (75)$$

$$\tilde{K}_{ij}(t) = O(r^2), \quad \partial_t \tilde{K}_{ij}(t) = O(r^2). \quad (76)$$

This argument suggests that if the lapse α and its derivatives do not introduce additional singularities at the punctures, and if there are no singularities appearing in the spatial derivatives of the metric (which we have not completely ruled out), then the right-hand sides of the evolution equations for $\tilde{\gamma}_{ij}$ and \tilde{K}_{ij} vanish at the punctures for all times. This means that $\tilde{\gamma}_{ij}$ and \tilde{K}_{ij} should not evolve at all at the punctures for a regular slicing and vanishing shift by construction, and the same is true for g_{ij} and K_{ij} .

C. Puncture evolutions in the BSSN system

For accurate finite differencing in the BSSN system for puncture data we split the logarithmic conformal factor ϕ into a singular but time-independent piece and an additional time-dependent contribution χ ,

$$\phi = \chi + \ln \psi_{BL}. \quad (77)$$

It remains to be seen whether χ and the remaining BSSN quantities are regular throughout the evolution, i.e. whether the coordinate singularity can be cleanly separated out with ψ_{BL} as in the case of ADM. To decide this issue we have to be specific about our gauge choice. In preparation for the discussion of the gauge for puncture evolutions in Sec. V we note some properties of the BSSN system near the punctures.

Each of the BSSN variables has the following initial value for puncture data at $t = 0$, which we assume to evolve as indicated by the arrows:

$$\chi = O(1) \rightarrow O(1), \quad (78)$$

$$K = 0 \rightarrow O(r^2), \quad (79)$$

$$\tilde{\gamma}_{ij} = O(1) \rightarrow O(1), \quad (80)$$

$$\tilde{A}_{ij} = O(r^3) \rightarrow O(r^2), \quad (81)$$

$$\tilde{\Gamma}^i = 0 \rightarrow O(r). \quad (82)$$

Assume furthermore that $\alpha = O(1)$, and that the derivatives of the $O(1)$ quantities are $O(1)$. Consider now the following form of the evolution equations, where we have inserted our assumptions for α , $\tilde{\gamma}_{ij}$, \tilde{A}_{ij} , and $\tilde{\Gamma}^i$, but have kept the explicit dependence on β^i , ϕ and K :

$$\partial_t \chi = \mathcal{L}_\beta \phi - \frac{1}{6} \alpha K, \quad (83)$$

$$\partial_t K = \mathcal{L}_\beta K + O(r^4)(O(1) + O(\partial\phi)) + \frac{1}{3} \alpha K^2, \quad (84)$$

$$\partial_t \tilde{\gamma}_{ij} = \mathcal{L}_\beta \tilde{\gamma}_{ij} + O(r^2), \quad (85)$$

$$\begin{aligned} \partial_t \tilde{A}_{ij} = & \mathcal{L}_\beta \tilde{A}_{ij} + KO(r^2) + O(r^4) (O(1) \\ & + O(\partial\phi) + O(\partial^2\phi) + O(\partial\phi)^2), \end{aligned} \quad (86)$$

$$\begin{aligned} \partial_t \tilde{\Gamma}^i = & -\partial_j \mathcal{L}_\beta \tilde{\gamma}^{ij} + O(r^2) + O(r^2)O(\partial\phi) \\ & - \frac{4}{3} \alpha \tilde{\gamma}^{ij} \partial_j K. \end{aligned} \quad (87)$$

If these equations are to hold for all times, to be checked by time stepping as in the last section, then we require certain assumptions about the shift as well. In particular, each of the terms involving \mathcal{L}_β should be of the same or higher order as the other terms in the corresponding equation, because otherwise there could be evolution towards lower orders in r . In particular, even assuming α and K are regular, we have to examine the behaviour of $\mathcal{L}_\beta \phi$ at the puncture before we can conclude that χ remains regular.

Let us assume that χ and its derivatives are regular, so that

$$\phi = O(\ln r), \quad \partial_i \phi = O(1/r), \quad \partial_i \partial_j \phi = O(1/r^2). \quad (88)$$

If furthermore $K = O(r^2)$, and if the shift terms are of sufficiently high order, then the right hand sides of (83)-(87) are at least $O(r)$. In this case, the order of each equation is such that the corresponding orders in (78)-(82) are maintained. In Sec. V we show that these assumptions can indeed be met by a proper gauge choice, and hence we arrive at the statement that in this case the punctures do not evolve by construction.

V. GAUGE CONDITIONS AND PUNCTURE EVOLUTIONS

The main question is whether there are lapse and shift conditions that behave appropriately for puncture evolutions. We will show that this is indeed the case without the need to introduce special boundary conditions at the punctures. What is required is an appropriately regularized implementation of our gauge conditions and a choice of initial data for lapse and shift such that the punctures do not evolve.

A. Lapse for puncture evolutions

Consider maximal slicing, which is implemented by choosing $K = 0$ at $t = 0$ and determining the lapse from the elliptic equation resulting from $\partial_t K = 0$, which for vanishing shift is

$$\Delta \alpha = \alpha K_{ij} K^{ij}. \quad (89)$$

As discussed in [7], for $g_{ij} = \psi_{BL}^4 \tilde{\gamma}_{ij}$,

$$\Delta \alpha = \psi_{BL}^{-4} \tilde{\Delta} \alpha - \delta^{ij} \Gamma_{ij}^k \partial_k \alpha, \quad (90)$$

so the principal part is degenerating to zero as $O(r^4)$. To avoid numerical problems we therefore multiply (89) by ψ_{BL}^4 , which normalizes the principal part but leaves a $O(1/r)$ term since $\Gamma_{ij}^k = O(1/r)$:

$$\tilde{\Delta} \alpha - O(1/r) \partial_k \alpha = O(r^6) \alpha. \quad (91)$$

It turns out that standard numerical methods to solve this elliptic equation will find a regular solution for α for which $\partial_k \alpha$ vanishes sufficiently rapidly so that $O(1/r) \partial_k \alpha$ is zero at the puncture. Therefore, maximal slicing and vanishing shift lead to a sufficiently regular lapse such that indeed the right-hand sides of the ADM evolution equations for $\tilde{\gamma}_{ij}$ and \tilde{K}_{ij} vanish at the punctures.

Effectively, maximal slicing implements the condition that the lapse has a vanishing gradient at the puncture. Notice that this condition is very different to an isometry-type condition, where the lapse would be forced to be -1 at the puncture. Fig. 1 shows a schematic representation in the Kruskal diagram of the type of slices one obtains in the case of a single Schwarzschild BH when using three different boundary conditions for the lapse (while keeping the same interior slicing condition): odd at the throat, even at the throat and zero gradient at the puncture. When looking at these plots it is important to keep in mind that the puncture corresponds to a compactification of the second asymptotically flat region, and is at an infinite distance to the left of the plots. Notice that, in all three cases, far away on the right hand side of the plot the slices approach the Schwarzschild slices (in fact, if we use maximal slicing and ask for the lapse to be odd we recover the Schwarzschild slices everywhere). Also, in the case with an odd lapse the slices do not penetrate the horizon, but in the other two cases they do.

Since maximal slicing is computationally expensive, we often use 1+log slicing that mimics the behaviour of the maximal lapse in that it also is singularity avoiding and the lapse drops to zero when the physical singularity approaches. Analytically, however, the 1+log lapse does not necessarily drop to zero at the puncture. Starting with $\alpha = 1$ and $K = 0$ everywhere at $t = 0$, we see from the evolution equations for the lapse and for K ,

$$\partial_t \alpha = -\alpha^2 f(\alpha) (K - K_0), \quad (92)$$

$$\partial_t K = \beta^i \partial_i K + \frac{1}{3} \alpha K^2 + O(r^3), \quad (93)$$

that neither α nor K evolve at the puncture if the shift or the derivative of K vanishes at the puncture. That means that the lapse will remain 1 at the puncture, and the inner asymptotically flat region will evolve. Numerically, one may expect this to be problematic if there is not sufficient resolution, as will be normally the case. The code can become unstable near the puncture, and even if it remains stable the event horizon may not prevent numerical inaccuracies to evolve into the outer regions. While this may happen, in practice the 1+log lapse does collapse, apparently precisely because of a lack of resolution, and the code remains stable. Even in this case we

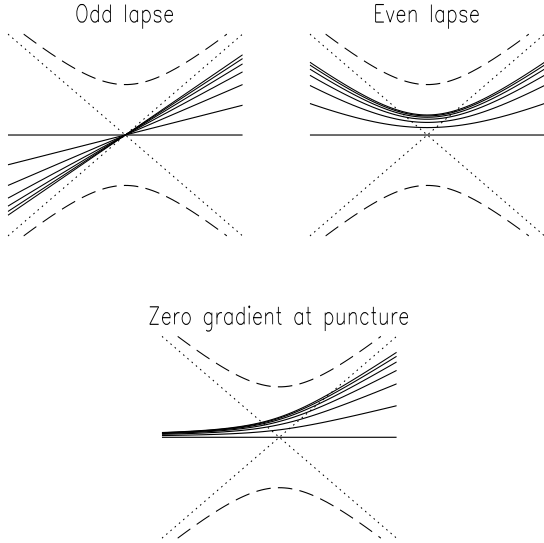


FIG. 1. Schematic representation on the Kruskal diagram of the effect of the different boundary conditions on the slices obtained. The first panel shows the case of an odd lapse at the throat, the second panel the case of an even lapse at the throat, and the last panel the case of a lapse with zero gradient at the puncture. The dashed lines show the singularities and the dotted lines the event horizon.

typically obtain convergence in the outer regions where the lapse did not collapse.

In this paper we experiment with 1+log slicing with $f(\alpha) = 2/\alpha$ replaced by $f(\alpha, \psi_{BL}) = 2\psi_{BL}^m/\alpha$, so that

$$\partial_t \alpha = -2\alpha \psi_{BL}^m (K - K_0), \quad (94)$$

i.e. we have introduced a factor that for $m > 0$ can drive the lapse to zero at the puncture. For $m = 0$ we obtain standard 1+log slicing. A natural choice is $m = 4$ since then the singularity in ψ_{BL}^4 exactly matches the degeneracy of the principal part of the second order wave equation associated with the lapse evolution, see (35) and (90). In particular, for $m = 4$ the wave speed is regular at the puncture.

Both choices of 1+log slicing with initial lapse equal to unity have been found to lead to stable evolutions of black holes with a lapse that satisfies the regularity conditions assumed in the previous sections. Another approach to obtain a vanishing lapse at the puncture is to start with a different initial lapse, for example

$$\alpha(t=0) = \psi_{BL}^{-2} = O(r^2), \quad (95)$$

so that the lapse is zero at the puncture initially and there is no evolution due to a non-vanishing lapse at the puncture. The power -2 is chosen so that the initial lapse has the same limit for $r \rightarrow \infty$ as the lapse $\alpha_{isotropic} = (1 - \frac{m}{2r})/(1 + \frac{m}{2r})$ of the static Schwarzschild metric in isotropic coordinates. In practice, we have found that with such an initial lapse there sometimes is too much

evolution in the still poorly resolved region between the puncture and the horizon, which is why we do not use this option routinely. Instead of guessing an initial lapse that minimizes the amount of initial evolution one should use the lapse (and shift) derived from a quasi-equilibrium thin-sandwich puncture initial data set, which however is currently not available.

B. Shift for puncture evolutions

For long term stable evolutions, we want to construct a shift condition that counters slice-stretching. However, for arbitrary non-vanishing shift, equations (83-87) show that the punctures will evolve. It is possible to have the punctures move across the grid because of a non-vanishing shift. One problem would be the numerical treatment of the coordinate singularity at the punctures, which so far was based on analytic derivatives of the time-independent conformal factor ψ_{BL} . While a solution of this problem may be possible, we focus here on finding a shift condition that counters slice-stretching while simultaneously satisfying a fall-off condition for the shift such that the punctures do not evolve at all when using the BSSN equations.

As a first step it is instructive to consider $\beta^i = rn^i = x^i = O(r)$ (with n^i a radial unit vector) near the puncture. In this case several terms in the Lie derivatives cancel exactly and we have

$$\mathcal{L}_{rn} \tilde{\gamma}_{ij} = x^k \partial_k \tilde{\gamma}_{ij}, \quad (96)$$

$$\mathcal{L}_{rn} \tilde{A}_{ij} = x^k \partial_k \tilde{A}_{ij}, \quad (97)$$

$$\mathcal{L}_{rn} K = x^k \partial_k K. \quad (98)$$

However,

$$\mathcal{L}_{rn} \phi = x^k \partial_k \chi + x^k \partial_k \ln \psi_{BL} + \frac{1}{2} = O(1), \quad (99)$$

so χ will evolve without a special combination of χ , K , and α . Furthermore, the Lie derivative will not be as simple if the shift is not exactly spherically symmetric.

We therefore turn to

$$\beta^i = O(r^3). \quad (100)$$

This happens to be the necessary condition (assuming integer powers of r) for the norm of the shift in the non-conformal metric to be zero at the puncture

$$\gamma_{ij} \beta^i \beta^j = O(1/r^4) \delta_{ij} \beta^i \beta^j. \quad (101)$$

With $\beta^i = r^3 n^i = r^2 x^i$ we now have

$$\mathcal{L}_{r^3 n} \tilde{\gamma}_{ij} = O(r^2) (x^k \partial_k \tilde{\gamma}_{ij} + \tilde{\gamma}_{ij}) = O(r^2), \quad (102)$$

$$\mathcal{L}_{r^3 n} \phi = O(r^2), \quad (103)$$

All other Lie derivative terms also turn out to be of order $O(r^2)$. Finally, the shift derivatives in the evolution equation for $\tilde{\Gamma}^i$ are

$$\partial_j \mathcal{L}_\beta \tilde{\gamma}^{ij} = \partial_j O(r^2) = O(r). \quad (104)$$

In this sense the evolution of $\tilde{\Gamma}^i$ poses the strictest condition on the fall-off of the shift.

The question remains how we guarantee the $O(r^3)$ fall-off in the actual shift condition. We can enforce such a fall-off by choosing

$$\beta^i(t=0) = 0, \quad (105)$$

and by changing the coefficient F in the hyperbolic Gamma-driver to

$$F(\alpha, \psi_{BL}) = \frac{3}{4} \alpha \psi_{BL}^{-n} = O(r^n), \quad (106)$$

where we typically choose $n = 2$ or 4 . Note that the two versions of the Gamma-driver differ by the term $\partial_t F/F = \partial_t \alpha/\alpha$, which in the case of 1+log slicing equals $-2\psi_{BL}^m(K - K_0)$. Let us ignore the diffusion term. If the shift has evolved into $\beta^i = O(r^3)$, then $\partial_t \tilde{\Gamma}^i = O(r)$. With $n \geq 2$ we have

$$\partial_t^2 \beta^i = O(r^3). \quad (107)$$

In fact, we have found that in the case of evolutions of just one black hole (distorted or not), changing F is not really necessary since there is enough symmetry in the problem to guarantee that the shift will have the correct fall-off at the puncture even without introducing the extra factor of ψ_{BL}^{-n} into F . When dealing with two black holes, however, this is no longer the case and the factor ψ_{BL}^{-n} is required to stop the shift from evolving at the punctures.

Anticipating the numerical results, let us point out that due to a lack of numerical resolution the shift often looks like $O(r)$ even though we have chosen $n = 2$ or 4 . Somewhat surprisingly, even in these cases the gauge conditions are able to approximately freeze the evolution, for which we do not yet have a good analytic explanation.

C. Vanishing of the shift at the punctures

Combining our choice of puncture initial data with the lapse and shift conditions above, we have the expectation that the BSSN variables will not evolve at the punctures. This is a natural situation considering that the punctures represent an asymptotically flat infinity, and that there is no linear momentum at the inner infinities. Performing the transformation $r \rightarrow 1/r$ for puncture data with the Bowen-York extrinsic curvature defined in (58) shows that the $1/r^3$ spin terms are mapped to $1/r^3$ terms, but the $1/r^2$ linear momentum terms are mapped to $1/r^4$ terms and there are no $1/r^2$ terms, and therefore there is no linear momentum at the inner infinity. In other words, viewed from the other asymptotic end, the black hole does not move in the data we use.

One can add a $1/r^4$ term to \tilde{A}_{ij} to make the holes move in the inner ends, but then the puncture initial data construction and the puncture evolutions on R^3 fail for a

lack of regularity at the punctures. In general, with a different choice of extrinsic curvature that does not satisfy the fall-off conditions of the Bowen-York data (58), there can be non-trivial or even singular evolution at the punctures in both the ADM and the BSSN systems.

In summary, our puncture initial data corresponds to two black holes which are momentarily at rest at their inner asymptotic ends. For a given coordinate system the black holes could start moving if there is a non-vanishing shift at the punctures, but we explicitly construct a vanishing shift at the punctures. The main consequence for puncture data of orbiting and colliding black holes is that by construction the inner asymptotic ends of the black hole will not move in our coordinate system, i.e. the punctures remain glued to the grid. That still allows for general dynamics around the punctures, which shows in the evolution of the metric and extrinsic curvature. For example, the apparent horizon can easily grow, drift and change shape, but it *can not* cross over the punctures for geometrical reasons, since the apparent horizon area would become infinite before they could do that. For orbiting black holes, since the punctures do not move by construction, it seems natural to combine the method of puncture evolutions with a corotating coordinate system to minimize the evolution of the metric data. We leave this option for future work.

VI. NUMERICS

The numerical time integration in our code uses an iterative Crank-Nicholson scheme with 3 iterations, see e.g. [40]. Derivatives are represented by second order finite differences on a Cartesian grid. We use standard centered difference stencils for all terms, except in the advection terms involving the shift vector (terms involving $\beta^i \partial_i$). For these terms we use second order upwind along the shift direction. We have found the use of an upwind scheme in such advection-type terms crucial for the stability of our code. Notice that this is the only place in our implementation where any information about causality is used (i.e. the direction of the tilt in the light cones).

A. Outer boundary condition

At the outer boundary we use a radiation (Sommerfeld) boundary condition. We start from the assumption that near the boundary all fields behave as spherical waves, namely we impose the condition

$$f = f_0 + u(r - vt)/r. \quad (108)$$

Where f_0 is the asymptotic value of a given dynamical variable (typically 1 for the lapse and diagonal metric components, and zero for everything else), and v is some wave speed. If our boundary is sufficiently far away one can safely assume that the speed of light is 1, so $v = 1$

for most fields. However, the gauge variables can easily propagate with a different speed implying a different value of v .

In practice, we do not use the boundary condition (108) as it stands, but rather we use it in differential form:

$$\partial_t f + v \partial_r f - v(f - f_0)/r = 0. \quad (109)$$

Since our code is written in Cartesian coordinates, we transform the last condition to

$$\frac{x_i}{r} \partial_t f + v \partial_i f + \frac{v x_i}{r^2} (f - f_0) = 0. \quad (110)$$

We finite difference this condition consistently to second order in both space and time and apply it to all dynamic variables (with possible different values of f_0 and v) at all boundaries.

There is a final subtlety in our boundary treatment. Wave propagation is not the only reason why fields evolve near a boundary. Simple infall of the coordinate observers will cause some small evolution as well, and such evolution is poorly modeled by a propagating wave. This is particularly important at early times, when the radiative boundary condition introduces a bad transient effect. In order to minimize the error at our boundaries introduced by such non-wavelike evolution, we allow for boundary behavior of the form:

$$f = f_0 + u(r - vt)/r + h(t)/r^n, \quad (111)$$

with h a function of t alone and n some unknown power. This leads to the differential equation

$$\begin{aligned} \partial_t f + v \partial_r f - \frac{v}{r} (f - f_0) &= \frac{v h(t)}{r^{n+1}} (1 - nv) + \frac{h'(t)}{r^n} \\ &\simeq \frac{h'(t)}{r^n} \quad \text{for large } r, \end{aligned} \quad (112)$$

or in Cartesian coordinates

$$\frac{x_i}{r} \partial_t f + v \partial_i f + \frac{v x_i}{r^2} (f - f_0) \simeq \frac{x_i h'(t)}{r^{n+1}}. \quad (113)$$

This expression still contains the unknown function $h'(t)$. Having chosen a value of n , one can evaluate the above expression one point away from the boundary to solve for $h'(t)$, and then use this value at the boundary itself. Empirically, we have found that taking $n = 3$ almost completely eliminates the bad transient caused by the radiative boundary condition on its own.

B. Fish-eye transformation

Setting up a reasonable numerical simulation, there is always the conflicting interest of having the boundary as far out as possible and having as good resolution as possible. With limited numerical resources it is almost never possible to obtain both at the same time. One way to

stretch limited resources as far as possible, is to introduce a radial coordinate transformation that decreases the resolution with distance. Such coordinate transformations can also be applied to 3D Cartesian grids, see the “fish-eye transformation” in [9,11].

In order to make the outer boundary conditions as simple as possible, we would like for the resolution to be constant at the location of the outer boundaries. That is, we want constant high resolution in the region containing the black holes, then we want a region where the resolution decreases with distance and finally we want a region (containing the outer boundaries) with constant low resolution. Denoting the physical radius by r and the coordinate radius by r_c , the previous requirements can be met with the following radial coordinate transformation

$$\begin{aligned} r = ar_c + (1 - a) \frac{s}{2 \tanh(\frac{r_0}{s})} &\left[\ln \left(\cosh \frac{r_c + r_0}{s} \right) \right. \\ &\left. - \ln \left(\cosh \frac{r_c - r_0}{s} \right) \right], \end{aligned} \quad (114)$$

where a is a parameter specifying the scale factor in grid spacing, r_0 is the radius of the transition region and s is the width of the transition region.

By differentiating r in equation (114) with respect to r_c we find that $dr/dr_c = 1$ for $r_c = 0$ and $dr/dr_c = a$ for $r_c \rightarrow \infty$ as required. Note that the radial r coordinate is mapped to ar_c plus a non-vanishing constant, and therefore the Jacobian of this transformation does not correspond to just a simple rescaling of radial resolution. The transformation (114) we refer to as the “transition fish-eye”.

An important point to keep in mind when using a fish-eye transformation is the fact that both the asymptotic values of metric components and the physical speed of light (and gauge speeds) will be affected by the transformation. This means that special care should be taken when applying boundary conditions.

VII. APPLICATIONS

In the numerical application of our method we focus on establishing the basic validity of the puncture evolutions with the hyperbolic shift. We consider evolutions of the spherically symmetric Schwarzschild spacetime, of a single distorted black hole, and of the head-on collision of two Brill-Lindquist punctures. We will report on orbiting binary systems elsewhere.

A. Evolution of a single Schwarzschild puncture

For the evolution of Schwarzschild we use the Cartoon method of [41] for implementing axisymmetric systems with 3D Cartesian finite differencing stencils. Choosing the z -axis as the axis of symmetry, we evolve a 3D Cartesian slab with just 5 points in the y -direction. On the

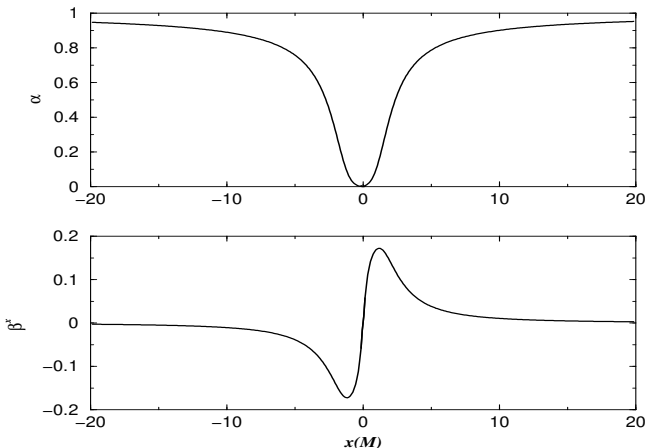


FIG. 2. Schwarzschild black hole evolved for $t = 1000M$. Shown are lapse α and shift component β^x along the x -axis, which are (anti-)symmetric about $x = 0$. By that time lapse and shift are approximately static. The lapse has collapsed to zero at the puncture and approaches one in the outer region. The shift crosses zero at the puncture, pointing away from the puncture and thereby halting the infall of points towards the puncture.

$y = 0$ plane standard 3D stencils are computed, and the data at the points with $y \neq 0$ are obtained by interpolation in the x -direction in the $y = 0$ plane and by tensor rotation about the z -axis. For Schwarzschild we also use the reflection symmetry in the $z = 0$ plane.

We choose the Schwarzschild puncture data of Sec. IV A with $m = 1.0M$ and the apparent horizon at $r = 0.5M$. As we have discussed, there are several choices for the gauge conditions. For the Schwarzschild puncture, we initialize lapse and shift to $\alpha = 1$ and $\beta^i = 0$. We consider 1+log slicing, (33), and the hyperbolic shift, (44), with the specific choice of

$$f = 2\alpha^{-1}\psi_{BL}^4, \quad F = \frac{3}{4}\alpha\psi_{BL}^{-2}, \quad \eta = 2.0/M. \quad (115)$$

In Fig. 2 we show lapse and shift for an evolution with 201 points in x - and z -direction, starting at the staggered point at the origin and extending to about $20M$ with a grid spacing of $0.1M$. We plot the data after an evolution of $t = 1000M$, which corresponds to 40000 time steps with a Courant factor of 0.25.

Lapse and shift show the characteristic feature of puncture evolutions. Both lapse and shift are zero at the puncture, indicating that there is no evolution at the inner asymptotically flat end of the black hole. The lapse approaches one in the outer region, while the shift points outward from the puncture and approaches zero in the outer region. The shift counters the infall of points towards the puncture, thereby stopping the slice stretching.

Fig. 3 shows various other quantities of the same

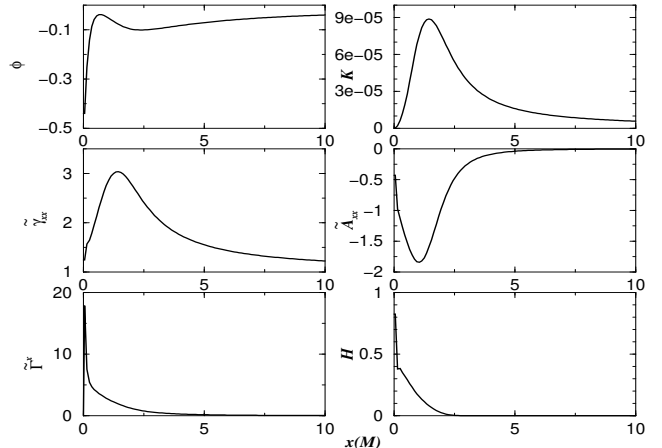


FIG. 3. Schwarzschild black hole evolved for $t = 1000M$. Shown are the BSSN variables ϕ , K , $\tilde{\gamma}_{xx}$, \tilde{A}_{xx} , and $\tilde{\Gamma}^x$ along the x -axis, and also the Hamiltonian constraint H .

Schwarzschild run at $t = 1000M$. Note the behaviour near the puncture, which at this resolution appears to be regular but is not sufficiently resolved.

In Fig. 4 we compare data from this run with a run for identical parameters except that instead of Eq. (44) we use Eq. (43) with $\eta = 2.8/M$ for the shift. The differences are quite small in the case of this Schwarzschild run.

In Fig. 5 we show the maximum of the shift and the root-mean-square value of the Hamiltonian constraint as a function of time. After a short time interval of less than $100M$ (recall that previous runs with vanishing shift lasted only to about $30\text{-}40M!$), evolution is approximately frozen for more than $3000M$. The observed drift in various quantities is crucially affected by the value of η that determines the diffusion in the hyperbolic Gamma-driver. In Fig. 5 we compare again the two versions of the Gamma-driver, and note that two different values of η , $2.0/M$ and $2.8/M$, are used to obtain long term stability. It is a matter of experimentation to find a suitable value of η in dependence on the various parameters in the run. Runs may crash before $100M$ for a bad choice of η . On the other hand, once determined for a particular initial data set and set of grid parameters, we found that the runs were rather robust under small variations. It would be useful to have a dynamic determination and adaptation of η , but this is currently not available.

Having established the basic features and the stability of our gauge choice, we want to study convergence for Schwarzschild. A crucial issue is whether we obtain convergence near the puncture. We choose three grid sizes and resolutions: 201 points in both the x - and z -directions for a resolution of $0.025M$, 401 points at $0.0125M$, and 801 points at $0.00625M$. With a Courant factor of 0.25 in the BSSN evolution scheme it takes 160, 320, and 640 iterations, respectively, for an evolution time of $1M$. The outer boundary is at about $5M$. We

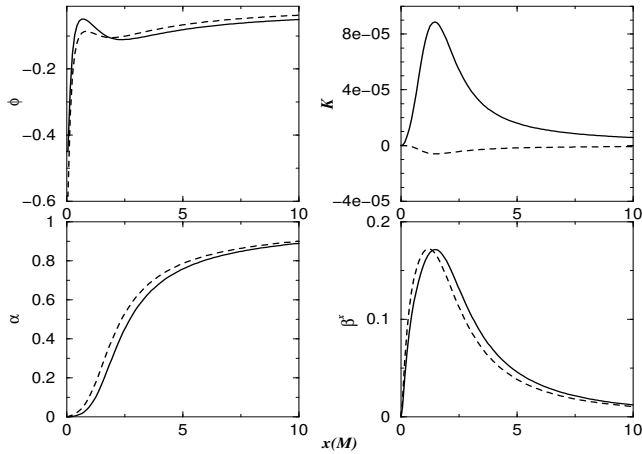


FIG. 4. Schwarzschild black hole evolved for $t = 1000M$. Shown is a comparison along the x -axis between two versions of the hyperbolic Gamma-driver for the shift, Eq. (43) (dashed line) and Eq. (44) (solid line).

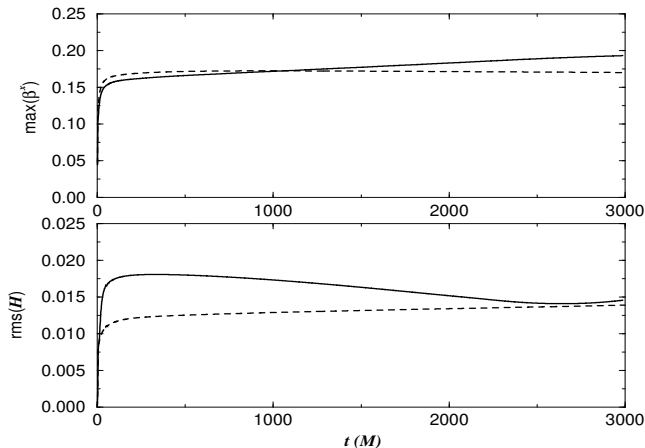


FIG. 5. Schwarzschild black hole evolved for $t = 3000M$. Shown are the maximum of the shift and the root-mean-square value of the Hamiltonian constraint as a function of time, again for two versions of the hyperbolic Gamma-driver for the shift, Eq. (43) (dashed line) and Eq. (44) (solid line), with diffusion parameter $\eta = 2.0/M$ and $\eta = 2.8/M$, respectively. After a short time interval during which lapse and shift adjust themselves dynamically, the evolution slows down significantly.

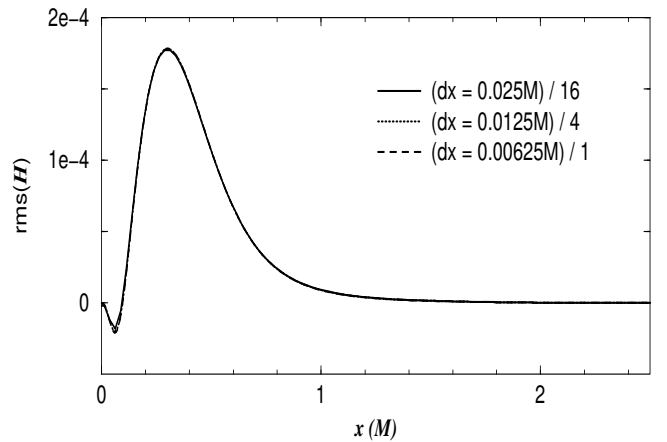


FIG. 6. Schwarzschild black hole evolved to $t = 5M$ at three high resolutions, demonstrating second order convergence at the puncture.

choose the same gauge as in (115), except that in F we use ψ_{BL}^{-4} instead of ψ_{BL}^{-2} for a broader profile of the shift near the puncture.

Fig. 6 shows the Hamiltonian constraint along the x -axis near the single Schwarzschild puncture at the three resolutions, rescaled by the corresponding factors expected for second order convergence. The coincidence of the three lines indicates clean second order convergence. Therefore, for such high resolutions the BSSN system exhibits the expected regular and convergent behaviour near the punctures. It is remarkable that even at a four times coarser resolution of $0.1M$ the evolutions remain stable.

Note in particular that the shift in Fig. 2 seems to be linear at the puncture, in contrast with the expected $O(r^3)$ behaviour. Fig. 7 shows the effect of different powers of ψ_{BL} in the shift equation for the grid parameters of the medium resolution run of the convergence test. We use the shift equation (44), and

$$F = \frac{3}{4}\alpha\psi_{BL}^{-n}, \quad \eta = 2.0/M, \quad (116)$$

with different values for n . Fig. 7 shows the shift for $t = 1M$. Note the resolution that is required to make the $O(r^3)$ behaviour visible for $n \geq 2$. By $t = 10M$, the shift for $n = 2$ is no longer completely resolved at the puncture with a grid spacing of $0.0125M$, but as we have seen, even at coarser resolutions the approximate $O(r)$ behaviour of the shift at the puncture allows stable evolutions.

B. Evolution of a single, distorted black hole

The second application we present is that of a distorted BH. Referring to [42], we choose a distortion parameter $Q_0 = 0.5$, position $\eta_0 = 0$, and width $\sigma = 1$. The ADM mass of this system is $M = 1.83$. Such data has been previously evolved in 2D and in 3D using excision. Here we discuss a 3D puncture evolution with octant symmetry, 129^3 points and a grid spacing of $0.1M = 0.183$. The

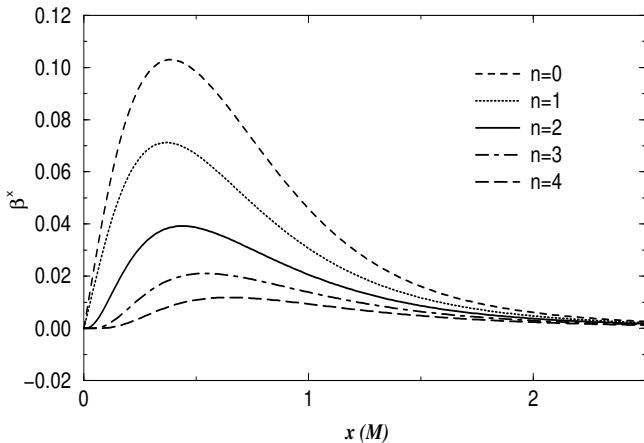


FIG. 7. Schwarzschild black hole evolved for $t = 1M$. Shown is the effect of varying the power n in ψ_{BL}^{-n} in the shift equation for β^x along the x -axis.

outer boundary is at about $12.8M$. For the gauge we use 1+log slicing with the initial lapse not unity but given by (95) and the hyperbolic shift condition (44) with

$$f = 2\alpha^{-1}\psi_{BL}^4, \quad F = \frac{3}{4}\alpha\psi_{BL}^{-2}, \quad \eta = 1.25/M \approx 0.68. \quad (117)$$

In Fig. 8, we show the evolution of the lapse and the shift component β^x along the x -axis. Note that the shift, although vanishing initially, develops the needed profile simply through its evolution equation, without any special initial condition. After a short while, the evolution effectively freezes, allowing the waves to propagate on an effectively fixed BH background, just as one would like.

For comparison, we show in Fig. 9 the evolution of the radial component of the metric, γ_{rr}/ψ_{BL}^4 , for the new gauge condition (lower panel) and for a singularity avoiding slicing run with 1+log slicing and vanishing shift (upper panel). For 1+log slicing and vanishing shift we see the well-known slice stretching effect. With the new gauge evolution is slowed significantly at late times. The peak of the metric near $x = 0.5M$ grows to about 12 by time $t = 20M$ and does not grow significantly after that until $t = 400M$ (lower panel), while for vanishing shift already at $t = 30M$ the peak in the metric has reached 40 without any sign of slowing growth (upper panel).

For the new gauge we expect that we can reliably extract the waveform for the ring-down, and this is indeed the case as shown in Fig. 10.

C. Head-on collision of two Brill-Lindquist punctures

The third application we present is that of a head on collision of two Brill-Lindquist BH's. The parameters for these simulations are $m_1 = m_2 = 0.5M$, $\mathbf{C}_1 = \{0, 1.1515M, 0\}$, $\mathbf{C}_2 = \{0, -1.1515M, 0\}$, where m_1 and m_2 are the masses of the BH's and \mathbf{C}_1 and \mathbf{C}_2 are the locations of the two punctures. These parameters correspond to an initial separation of the BH's equal

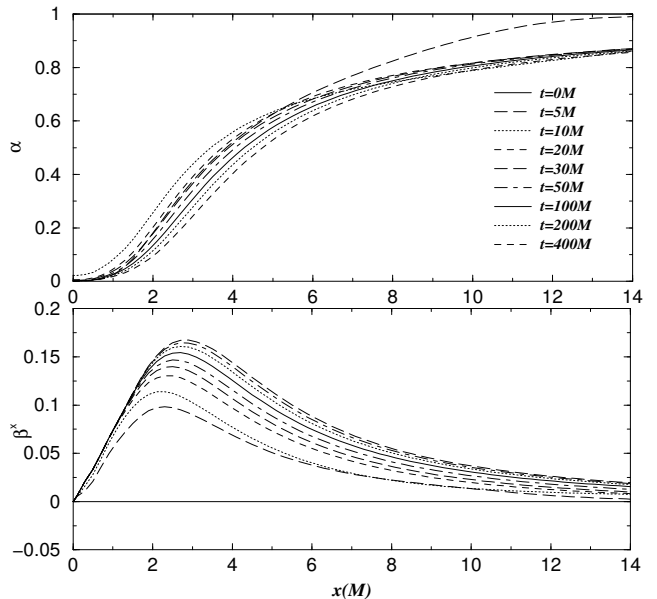


FIG. 8. Lapse and shift for the evolution of a single distorted BH. After around $20M$, the evolution of lapse and shift slows down significantly (note the time labels). The approach to the final profile in lapse and shift is not monotonic.

to that of an approximate ISCO configuration as determined in [43]. Such data has been previously evolved without shift with the Lazarus technique that combines short, fully numerical evolutions with a close limit approximation for the wave extraction [9] (see [12] for runs starting at larger separation).

We present two types of runs for the head-on collision starting at the approximate ISCO separation. In the first type we use 1+log slicing and the hyperbolic Gamma-driver (43) with

$$f = 2\alpha^{-1}, \quad F = \frac{3}{4}\alpha\psi_{BL}^{-4}, \quad \eta = 2.8/M. \quad (118)$$

with an initial lapse equal to one and an initial shift equal to zero. We also use the transition fish-eye with parameters $a = 3$, $s = 1.2M$ and $r_0 = 5.5M$. This places the outer boundary at a distance of $25.8M$ with central resolutions $0.128M$, $0.064M$ and $0.032M$ and gridsizes 96^3 , 192^3 and 384^3 respectively in octant mode.

In Fig. 11 we show the extracted $\ell = 2$ and $m = 0$ waveforms until $t = 80M$ for all three resolutions. The code actually continued beyond $t = 140M$ at the highest resolution (more than $t = 200M$ at the lower resolutions) before we stopped it, due to the fact that it was computationally fairly expensive. Initially there seem to be some small amplitude oscillations superposed on the larger oscillations. These seem to be related to an initial wave pulse in the lapse moving outwards as the lapse collapses from its initial value, which is not quite handled by the wave extraction procedure. However these oscillations decrease with increasing resolution. With $f = 2\alpha^{-1}\psi_{BL}^4$

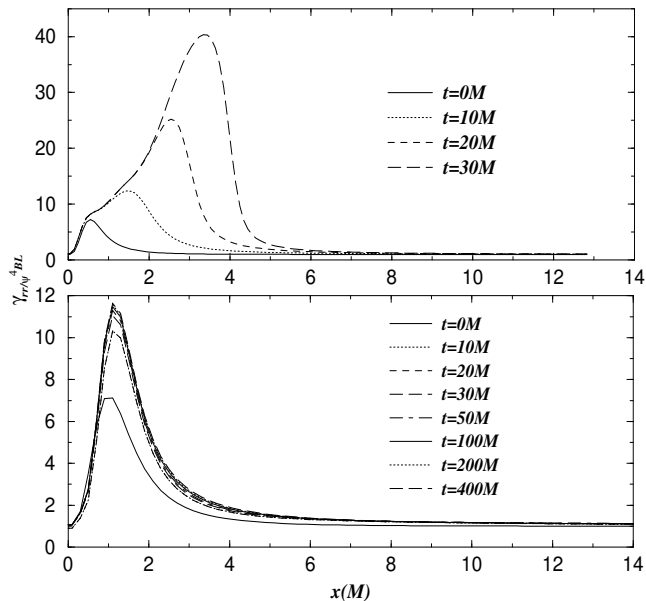


FIG. 9. The evolution of the radial metric function γ_{rr}/ψ_{BL}^4 for a distorted BH along the x -axis. The upper panel shows the slice stretching in the metric for singularity avoiding slicing with vanishing shift, while the lower panel shows the metric for the new gauge conditions. Without shift the metric grows out of control after $t = 40M$, while with the new shift condition a peak begins to form initially but later almost freezes as lapse and shift drive the BH into an essentially static configuration (note the time labels).

as we used in the previous examples instead of (118), the oscillations are larger, probably because the lapse is more dynamic in the initial phase of the evolution. But as already mentioned in Sec. V A, even with $f = 2\alpha^{-1}\psi_{BL}^0$ the lapse collapses at the punctures. After about $t = 80M$ we see some non-quasi-normal features in the waveform, that are most probably due to contaminations from the outer boundary.

For a wave signal A extracted at three resolutions, Δ , 2Δ and 4Δ the order of convergence, σ , can be estimated as

$$\sigma = \log_2 \left| \frac{A(4\Delta) - A(2\Delta)}{A(2\Delta) - A(\Delta)} \right|. \quad (119)$$

In Fig. 12 we show this estimate of the convergence factor for the three waveforms from Fig. 11. Several features in this figure deserve comment. First of all, for the first $15M$ the signal is very small, so the estimate of the convergence order is not very accurate. Secondly, the phase evolution of the waveforms is somewhat resolution dependent. This means that the curves cross over each other at different times, leading to the spikes clearly visible in the plot. The differences in phase evolution seem to decrease with increasing resolution, although only at somewhere between first and second order. However excluding the initial part and the spikes, we see a reasonable second order convergence in the waveforms up to $t = 80M$.

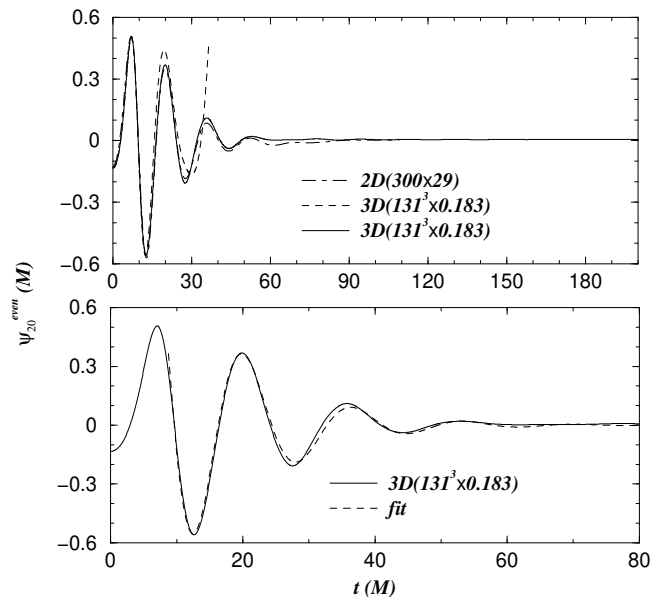


FIG. 10. The solid line shows the $\ell = 2, m = 0$ waveform extracted at a radius of $5.45M$ for the even-parity distorted BH described in the text, while the two dashed lines show the result of the same simulation carried out in the 2D and 3D code with vanishing shift. The 2D code crashes at around $t = 100M$ and the 3D code crashes around $t = 40M$. The lower panel shows a fit for the time interval from $t = 9M$ to $t = 80M$ to the two lowest quasi normal modes of the BH for the new gauge conditions in 3D, confirming that the ring-down of the distorted BH is simulated accurately.

In Table I, we try to circumvent the problem of the differently evolving phase by locating the extrema of the waveforms and estimating the convergence order using these extremal values even if they do not occur at the same time. As can be seen, except for the first maximum, there is generally nice second order convergence in the amplitude. In the case of the first maximum, it can be seen from Fig. 11 that the difference between the three resolutions is very small and that especially the lowest resolution is influenced by the pulse in the lapse moving out.

As a second type of gauge choice we use maximal slicing and the hyperbolic gamma driver condition with the

Extremum	$\log_2 (A(4\Delta) - A(2\Delta))/(A(2\Delta) - A(\Delta)) $
1	1.17
2	2.11
3	2.00
4	1.95
5	1.96
6	2.24

TABLE I. The convergence of the amplitude for the first six local extrema of the extracted $\ell = 2, m = 0$ waveforms for the head on collision of two Brill-Lindquist BH's extracted at radius $18.5M$.

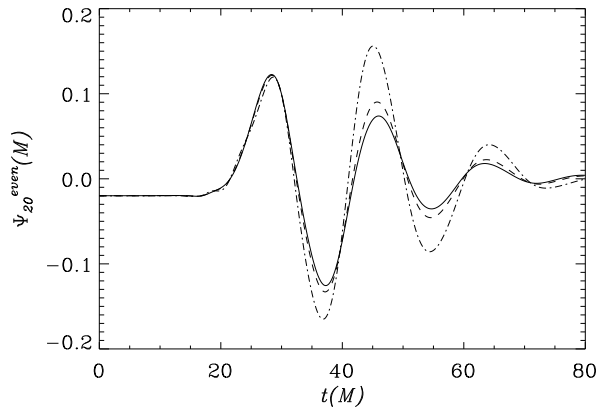


FIG. 11. The extracted $\ell = 2$, $m = 0$ waveforms for the head on collision of two Brill-Lindquist BH's at three different resolutions extracted at $18.5M$. The resolutions for the solid, dashed and dash-dotted line are $0.032M$, $0.064M$ and $0.128M$ respectively.

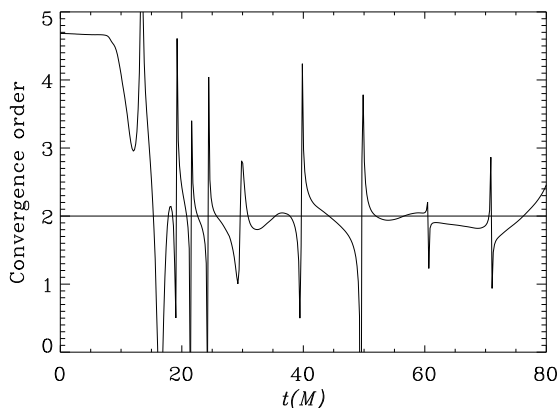


FIG. 12. The convergence order in the extracted $\ell = 2$, $m = 0$ waveforms for the head on collision of two Brill-Lindquist BH's extracted at $18.5M$, based on the same three resolutions ($0.032M$, $0.064M$, $0.128M$) as in Fig. 11.

same shift parameters as in the 1+log case, except for the fact that $\eta = 2.0/M$ here. In this case the resolution is $0.128M$ and the grid size is 80^3 in octant mode. The fish-eye parameters are $a = 4$, $s = 1.2M$ and $r_0 = 5.0M$ placing the outer boundary at a distance of $26M$. This run ran for about a month on two processors on a dual 1.7 GHz Xeon workstation reaching $t = 5224M$, until the machine went down due to an unrelated problem. By that time, the evolution was almost completely frozen as can be seen from Fig. 13 showing the common apparent horizon mass as function of time. Most of the evolution occurs before $t = 200M$ and after that there is just a slow drift of the apparent horizon mass giving about 10% error at $t = 5000M$.

In Fig. 14 we plot the extracted waveform with a logarithmic time scale (actually $\ln(t+1)$) in order to be able to see the features in the beginning of the waveform, while

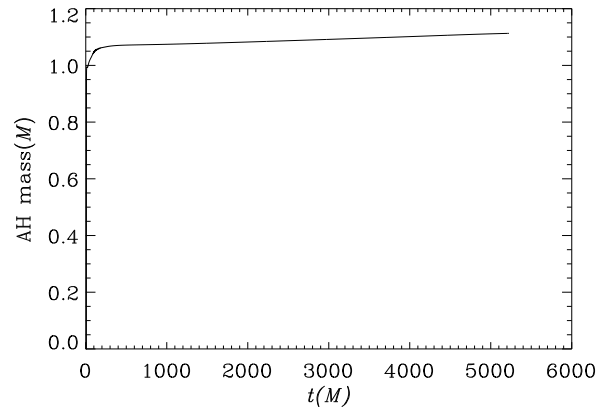


FIG. 13. The apparent horizon mass for the head on collision of two Brill-Lindquist BH's with maximal slicing.

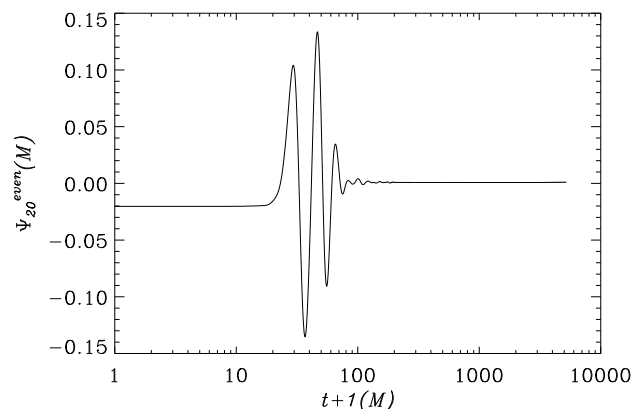


FIG. 14. The extracted $\ell = 2$, $m = 0$ waveforms for the head on collision of two Brill-Lindquist BH's with maximal slicing. Note that we plot $t + 1$ in order to be able to use a logarithmic scale on the time axis.

still showing that it is constant and very close to zero at $t = 5000M$. The features in the initial part of this waveform are very similar to the features in the 1+log run of the same resolution. However it is completely smooth in the initial phase, where the 1+log waveform has the small amplitude oscillations, since with an elliptic lapse condition, there is no wave pulse in the lapse moving outwards.

As mentioned before, these evolutions were done in octant symmetry. We repeated the maximal slicing evolution in bitant symmetry (reflection about one coordinate plane), with exactly the same physical and gauge parameters. However, this evolution died at about $t = 280M$, showing some clearly asymmetric features in the lapse and metric components in the directions where the symmetry is not imposed. We first encountered such a dependence of the stability of the BSSN system on the octant symmetry in excision runs of a single black hole [16]. The current result supports the conclusion that the stability problem is not directly linked to the excision technique or

the gauge conditions, but is probably intrinsic to BSSN. We are currently investigating the cause of this problem.

In conclusion, with the new gauge conditions we can evolve not only single black hole systems but also the head on collision of two black holes with dynamically adjusting lapse and shift and reach an almost static solution for the final black hole. While we have argued in detail why the punctures should not evolve, and while it is plausible that there is sufficient freedom in the gauge to almost freeze the evolution of a single, spherical black hole, it is remarkable that the method is successful even in the region close to and between two black holes.

VIII. CONCLUSION

We have discussed a new family of coordinate conditions for 3D numerical relativity that are powerful, efficient, easy to implement, and respond naturally to the spacetime dynamics. An application of these conditions to previously difficult BH spacetimes shows their strength: even without excision, they allow distorted and colliding BH spacetimes to be evolved for more than two orders of magnitude longer than possible previously, for thousands of M rather than tens of M , while keeping errors down to a few percent and allowing accurate waveform extraction. The evolution methods and gauge choices discussed here have already passed preliminary tests for orbiting punctures. Work is in progress to modify the shift condition for corotating coordinates.

ACKNOWLEDGMENTS

We would like to thank J. Baker for useful discussions and comments. The numerical experiments were implemented using BAM and the Cactus Computational Toolkit [44,45]. The computations were performed at the Max-Planck-Institut für Gravitationsphysik, on the Platinum linux cluster at NCSA, on the Hitachi SR8000-F1 at the Leibniz-Rechenzentrum of the Bavarian Academy of Sciences and on the IBM SP at the National Energy Research Scientific Computing Center (NERSC). This work was supported in part by the EU Programme ‘Improving the Human Research Potential and the Socio-Economic Knowledge Base’ (Research Training Network Contract HPRN-CT-2000-00137).

[1] L. Smarr, Ph.D. thesis, University of Texas, Austin, Austin, Texas, 1975.
 [2] L. Smarr, *Ann. N. Y. Acad. Sci.* **302**, 569 (1977).
 [3] P. Anninos *et al.*, *Phys. Rev. Lett.* **71**, 2851 (1993).

[4] C. Bona, J. Massó, E. Seidel, and J. Stela, *Phys. Rev. Lett.* **75**, 600 (1995).
 [5] P. Walker, Ph.D. thesis, University of Illinois at Urbana-Champaign, Urbana, Illinois, 1998.
 [6] P. Anninos *et al.*, *Phys. Rev. D* **52**, 2059 (1995).
 [7] B. Brügmann, *Int. J. Mod. Phys. D* **8**, 85 (1999).
 [8] M. Alcubierre *et al.*, *Phys. Rev. Lett.* **87**, 271103 (2001), gr-qc/0012079.
 [9] J. Baker, B. Brügmann, M. Campanelli, and C. O. Lousto, *Class. Quantum Grav.* **17**, L149 (2000).
 [10] J. Baker *et al.*, *Phys. Rev. Lett.* **87**, 121103 (2001).
 [11] J. Baker, M. Campanelli, and C. O. Lousto, *Phys. Rev. D* **65**, 044001 (2002).
 [12] J. Baker, M. Campanelli, C. O. Lousto, and R. Takahashi, *Phys. Rev. D* **65**, 124012 (2002), astro-ph/0202469.
 [13] J. Thornburg, *Class. Quan. Grav.* **4**, 1119 (1987).
 [14] E. Seidel and W.-M. Suen, *Phys. Rev. Lett.* **69**, 1845 (1992).
 [15] R. Gomez *et al.*, *Phys. Rev. Lett.* **80**, 3915 (1998).
 [16] M. Alcubierre and B. Brügmann, *Phys. Rev. D* **63**, 104006 (2001), gr-qc/0008067.
 [17] S. Brandt *et al.*, *Phys. Rev. Lett.* **85**, 5496 (2000).
 [18] M. Alcubierre *et al.*, *Phys. Rev. D* **64**, R61501 (2001), gr-qc/0104020.
 [19] D. Brill and R. Lindquist, *Phys. Rev.* **131**, 471 (1963).
 [20] J. York, in *Sources of Gravitational Radiation*, edited by L. Smarr (Cambridge University Press, Cambridge, England, 1979).
 [21] T. W. Baumgarte and S. L. Shapiro, *Physical Review D* **59**, 024007 (1999).
 [22] M. Shibata and T. Nakamura, *Phys. Rev. D* **52**, 5428 (1995).
 [23] M. Alcubierre *et al.*, *Phys. Rev. D* **62**, 124011 (2000), gr-qc/9908079.
 [24] L. Andersson and V. Moncrief, (1998), unpublished.
 [25] L. Andersson and V. Moncrief, *Ann. H. Poincare* (2001), submitted, gr-qc/0110111.
 [26] D. Garfinkle and C. Gundlach, *Class. Quantum Grav.* **16**, 4111 (1999), gr-qc/9908016.
 [27] P. R. Brady, J. D. E. Creighton, and K. S. Thorne, *Phys. Rev. D* **58**, 061501 (1998).
 [28] J. Balakrishna *et al.*, *Class. Quantum Grav.* **13**, L135 (1996).
 [29] M. Alcubierre, *Phys. Rev. D* **55**, 5981 (1997).
 [30] M. Alcubierre and J. Massó, *Phys. Rev. D* **57**, 4511 (1998).
 [31] L. Smarr and J. York, *Phys. Rev. D* **17**, 2529 (1978).
 [32] A. Lichnerowicz, *J. Math Pures et Appl.* **23**, 37 (1944).
 [33] C. Misner and J. Wheeler, *Ann. Phys. (N.Y.)* **2**, 525 (1957).
 [34] R. Beig and N. O’Murchadha, *Class. Quantum Grav.* **13**, 739 (1996).
 [35] S. Brandt and B. Brügmann, *Phys. Rev. Lett.* **78**, 3606 (1997).
 [36] S. Dain, C. O. Lousto, and R. Takahashi, *Phys. Rev. D* **65**, 104038 (2002), gr-qc/0201062.
 [37] S. Dain, *Phys. Rev. Lett.* **87**, 121102 (2001), gr-qc/0012023.
 [38] S. Dain and H. Friedrich, *Comm. Math. Phys.* **222**, 569

- (2001), gr-qc/0102047.
- [39] S. Dain, Phys. Rev. D (to be published) (2001), gr-qc/0103030.
 - [40] M. Alcubierre *et al.*, Phys. Rev. D **62**, 044034 (2000), gr-qc/0003071.
 - [41] M. Alcubierre *et al.*, Int. J. Mod. Phys. D **10**, 273 (2001), gr-qc/9908012.
 - [42] S. Brandt, K. Camarda, and E. Seidel, in *Proceedings of the 8th Marcel Grossmann Meeting on General Relativity*, edited by T. Piran (World Scientific, Singapore, 1999), pp. 741–743.
 - [43] T. W. Baumgarte, Phys. Rev. D **62**, 024018 (2000).
 - [44] B. Brügmann, Ann. Phys. (Leipzig) **9**, 227 (2000), gr-qc/9912009.
 - [45] Cactus, <http://www.cactuscode.org>.